International Journal of Thermophysics, Vol. 21, No. 1, 2000

Thermophysical Properties of Gaseous Tungsten Hexafluoride from Speed-of-Sound Measurements

J. J. Hurly[1]

Received August 13, 1999

The speed of sound was measured in gaseous WF_6 using a highly precise acoustic resonance technique. The data span the temperature range from 290 to 420 K and the pressure range from 50 kPa to the lesser of 300 kPa or 80% of the sample's vapor pressure. At 360 K and higher temperatures, the data were corrected for a slow chemical reaction of the WF_6 within the apparatus. The speed-of-sound data have a relative standard uncertainty of 0.005%. The data were analyzed to obtain the ideal-gas heat capacity as a function of the temperature with a relative standard uncertainty of 0.1%. These heat capacities are in reasonable agreement with those determined from spectroscopic data. The speed-of-sound data were fitted by virial equations of state to obtain the temperature dependent density virial coefficients. Two virial coefficient models were employed, one based on square-well intermolecular potentials and the second based on a hard-core Lennard–Jones intermolecular potential. The resulting virial equations reproduced the sound-speed data to within ± 0.005% and may be used to calculate vapor densities with relative standard uncertainties of 0.1% or less. The hard-core Lennard–Jones potential was used to estimate the viscosity and the thermal conductivity of dilute WF_6. The predicted viscosities agree with published data to within 5% and can be extrapolated reliably to higher temperatures.

KEY WORDS: equation of state; intermolecular potential; speed-of-sound; thermodynamic properties; transport properties; tungsten hexafluoride; virial coefficients; viscosity; WF_6.

1. INTRODUCTION

As part of the National Semiconductor Metrology Program, our laboratory has developed novel acoustic techniques to characterize the hazardous

[1] Physical and Chemical Properties Division, Chemical Science and Technology Laboratory National Institute of Standards and Technology, Gaithersburg, Maryland 20899, U.S.A.

and corrosive gases used to process semiconductors. Better-characterized process gases will result in greater control over the manufacturing process. Tungsten hexafluoride (WF_6) is used in the semiconductor industry for the chemical vapor deposition (CVD) of tungsten silicide layers on silicon wafers. Tungsten hexafluoride is reactive, decomposing in the presence of moisture to produce hydrofluoric acid. Here we report speed-of-sound data $u(T, P)$ for gaseous WF_6. From the $u(T, P)$ data, we deduce the ideal-gas heat capacity, the equation of state, and the viscosity of the dilute gas. Figure 1 shows the vapor pressure curve [1], the critical point, and each state point where the speed of sound was measured. The triple-point temperature of tungsten hexafluoride is approximately 275 K [2], and its critical parameters have been reported as $T_c = 452.7$ K, $P_c = 4.57$ MPa, and $\rho_c = 1.28\ \mathrm{g \cdot cm^{-3}}$ [3]. Tungsten hexafluoride's octahedral symmetry can be reasonably approximated by a spherically symmetric intermolecular potential model. In Sections 7 and 8 below, we provide model intermolecular potentials.

The speed-of-sound data span the ranges $290\ \mathrm{K} \leqslant T \leqslant 420\ \mathrm{K}$ and $50\ \mathrm{kPa} \leqslant P \leqslant 300\ \mathrm{kPa}$. The measurements were made along isotherms. At the lowest pressure on each isotherm and at selected other pressures, the

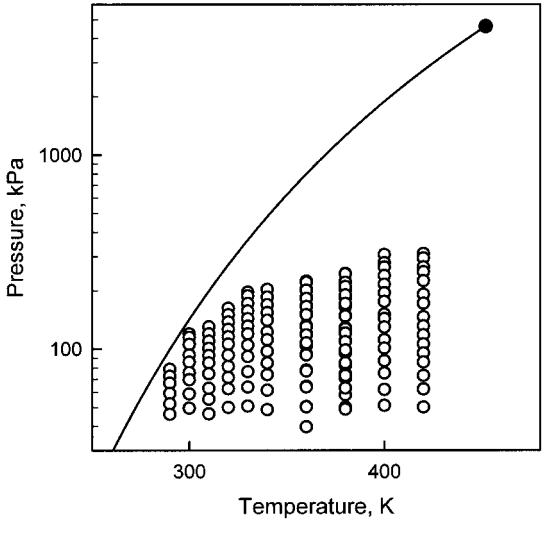

Fig. 1. Locations of speed-of-sound data with respect to the saturated vapor pressure [1] and the critical point [3]. Each measured state point is shown as an open circle.

temperature was held constant and the sound speed measured as a function of time, t. At 360 K and higher temperatures, the speed of sound slowly increased. This increase was attributed to a slow chemical reaction within the apparatus which progressively lowered the average molecular weight of the sample. The data along each isotherm at 360 K and higher temperatures were corrected for this reaction. The corrections were independently determined for each temperature and each gas sample. After the correction, the relative standard uncertainty (unless otherwise noted, coverage factor σ or $k = 2$) of the sound speeds was 0.005 %. From the zero-pressure intercepts of the isotherms, the constant-pressure ideal-gas heat capacity $C_p^0(T)$ was calculated. These C_p^0 values have relative standard uncertainties of 0.1 %. The complete set of $u(T, P)$ data was fitted by virial equations of state to determine the temperature dependent second and third density virial coefficients $B(T)$ and $C(T)$. Two models for the virial coefficients were used, the hard-core square-well (HCSW) model and the hard-core Lennard–Jones (HCLJ) model. Both virial equations of state reproduced the speed-of-sound data with a relative standard uncertainty of 0.001 %. Gillis and Moldover [4] have shown that the gas density ρ calculated from a virial equation of state as determined from experimental sound speeds will have a relative standard uncertainty of less than 0.1 %. The use of model intermolecular potentials to represent the virial coefficients allows the equation of state to be reliably extrapolated to temperatures well above our experimental range.

The advantage of the HCSW model is that it is easy to use. Since the virial coefficients are simple algebraic functions of temperature, the virial coefficients and their temperature derivatives may be directly evaluated. However, different potential parameters for $B(T)$ and $C(T)$ are necessary to take advantage of the full precision of the data. The HCLJ model is based on a more realistic intermolecular potential and has the advantage of having fewer parameters. The potential is an accurate representation of two interacting WF_6 molecules from which both $B(T)$ and $C(T)$ can be determined, which is the physical reality. The result is a more accurate extrapolation to higher temperatures. However, the virial coefficients and their temperature derivatives for this model must be calculated by numerical integration. To make the HCLJ model easier to use, a look-up table is supplied from which $B(T)$ and $C(T)$ and their temperature derivatives may be calculated with a simple interpolation routine.

It has been shown that the transport properties, such as dilute-gas viscosities, calculated from the derived HCLJ potential should be accurate to within 10 % throughout the temperature range from the triple point to in excess of 1000 K [5]. The calculated viscosities for WF_6 are within 5 % of the one set of experimental values [6].

2. EXPERIMENTAL TECHNIQUE

We use a highly precise acoustic resonance technique to determine the speed of sound in a gas. The resonance frequencies f within a cylindrical cavity (or resonator) containing the sample gas are measured as a function of temperature and pressure. Reference 5 provides a description of the current apparatus including the modifications made for handling reactive and hazardous gases. An earlier version was used to study more than 20 nonhazardous gases and gas mixtures [7, 8]. The acoustic model is described in Refs. 9 and 10.

The temperature-dependent effective radius $a(T)$ and length $l(T)$ of the cylindrical resonator were required to determine the speed of sound from the measured resonance frequencies. These dimensions were determined from the measured resonance frequencies as functions of the temperature with the resonator filled with argon, a gas for which the speed of sound is accurately known. Because the calibration and the final measurements were conducted in the same thermostated bath, there is a high degree of compensation for the effects of temperature gradients in the bath and even for systematic errors in the measurement of temperature.

At each state point the frequency of the sound generator was stepped through the resonances, and the amplitude and phase of the signal from the detector were recorded. Measurements were made at 11 frequencies spanning $f_{\mathrm{KNS}} \pm g_{\mathrm{KNS}}$, where g is the half-width, for each mode (K, N, S). The modes are labeled with the notation (K, N, S) of Gillis [9]. The theoretically expected function was then fitted to the amplitudes and phases measured at each frequency to obtain both f_{KNS} and g_{KNS} and a measure of their uncertainties. Typically, the standard deviation of f_{KNS} was less than $10^{-5} f_{\mathrm{KNS}}$. The speed of sound u in the sample gas is determined from the measured resonance frequencies f_{KNS} by $u = 2\pi f_{\mathrm{KNS}}/k_{\mathrm{KNS}}$. For a cylindrical cavity with a radius a and length l, discrete values of the wavenumber k_{KNS} are known [11]. The measured resonance frequencies were corrected [9, 10] for the thermal and viscous losses at the boundaries as well as for the small effects of the duct used to move sample into and out of the resonance cavity.

The zero-pressure limiting value of the speed of sound is $u_0^2 = (C_p^0/C_v^0)\, RT/m$. Because u_0^2 is inversely proportional to the molecular weight m of the gas (m for WF_6 is 297.84 $\mathrm{g \cdot mol^{-1}}$), extreme care had to be taken to maintain the sample purity. Initially, the resonator was maintained at the lowest temperature, 290 K, and flushed several times with WF_6 until two successive loadings reproduced resonance frequencies within the experimental uncertainties. The resonance frequencies were then recorded along isotherms. At the end of each isotherm, the pressure was maintained

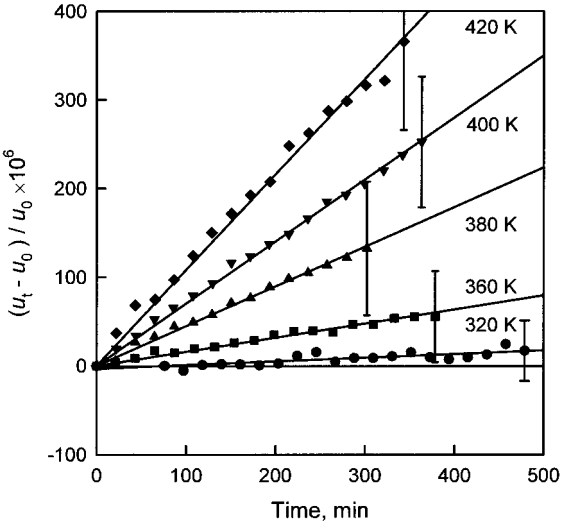

Fig. 2. Time dependence of the speed of sound in WF_6 at 50 kPa as a function of temperature. The solid lines are linear least-square fits.

at 50 kPa and the speed of sound was measured every 20 min for approximately 300 min, the interval required to characterize the isotherm. At temperatures below 360 K, the speed of sound remained constant within the experimental uncertainties. At temperatures of 360 K and higher, the speed of sound increased linearly with time, indicating a progressive decrease of the average molecular weight, presumably from a chemical reaction. Further analysis showed that the apparent reaction rate varied approximately as P^{-1}. This is consistent with WF_6 either reacting or decomposing in a surface catalyzed reaction. Figure 2 shows how the speed of sound changed with time. As discussed in Section 5, the isotherms of 360 K and higher were corrected for this composition shift.

3. PROCEDURES

The WF_6 sample was obtained from a commercial vendor and was certified VLSI (very large-scale integration) grade, 99.9995% purity (volume fraction). At each temperature the resonator was initially loaded with WF_6 to the lesser of 300 kPa or 80% of the vapor pressure. A fresh sample of WF_6 was used for each filling. The frequencies and widths of the first and second radial modes and the third and fourth longitudinal modes were measured at each pressure–temperature state point. The temperature

Table I. Speed of Sound in WF_6

P (kPa)	u ($m \cdot s^{-1}$)	$\sigma[u]/u$ $\times 10^6$	P (kPa)	u ($m \cdot s^{-1}$)	$\sigma[u]/u$ $\times 10^6$	P (kPa)	u ($m \cdot s^{-1}$)	$\sigma[u]/u$ $\times 10^6$
$T = 290$ K			$T = 310$ K			$T = 330$ K		
96.46	90.6767	49	130.39	93.4326	27	196.31	95.5961	17
88.85	90.8967	41	119.86	93.6840	33	187.90	95.7669	20
78.69	91.1883	45	110.00	93.9153	35	171.93	96.0900	25
72.50	91.3610	43	100.96	94.1265	35	157.10	96.3841	29
66.84	91.5191	42	92.57	94.3202	36	143.60	96.6511	30
59.13	91.7327	39	84.93	94.4963	35	131.21	96.8936	31
52.27	91.9213	42	74.62	94.7313	37	119.88	97.1136	35
46.20	92.0865	42	62.80	94.9996	35	104.76	97.4053	35
			55.18	95.1719	31	91.52	97.6591	38
			46.42	95.3665	49	76.42	97.9458	39
						63.72	98.1849	39
						50.83	98.4268	41
$T = 300$ K			$T = 320$ K			$T = 340$ K		
119.81	91.8800	39	162.32	94.5072	46	202.80	97.2571	25
114.89	92.0096	38	150.40	94.7650	26	185.42	97.5759	26
105.69	92.2492	39	138.00	95.0363	32	169.16	97.8723	27
93.32	92.5688	40	126.43	95.2850	33	154.25	98.1419	35
85.82	92.7604	39	115.82	95.5112	34	140.69	98.3852	38
75.64	93.0173	38	106.07	95.7179	35	122.57	98.7079	40
69.54	93.1704	42	92.98	95.9929	36	111.69	98.8999	42
58.77	93.4394	42	81.45	96.2335	36	97.33	99.1519	45
49.67	93.6651	40	71.32	96.4428	45	84.74	99.3715	48
			62.45	96.6260	40	73.77	99.5626	47
			50.07	96.8806	36	61.35	99.7767	50
						48.74	99.9939	50

was maintained, and the pressure was reduced in successive steps. For each pressure step, air-operated valves were opened briefly and a portion of the sample gas was collected in a reservoir immersed in liquid nitrogen. Once the pressure was reduced, the resonator was allowed to return to equilibrium and the frequencies and widths were measured at the new state point. This process continued until the pressure reached 50 kPa, where the pressure and temperature were maintained, and a measurement taken approximately every 20 min for 300 min.

Table I. *(Continued)*

P (kPa)	u ($m \cdot s^{-1}$)	$\sigma[u]/u$ $\times 10^6$	P (kPa)	u ($m \cdot s^{-1}$)	$\sigma[u]/u$ $\times 10^6$	P (kPa)	u ($m \cdot s^{-1}$)	$\sigma[u]/u$ $\times 10^6$
$T = 360$ K[a]			$T = 380$ K[a]			$T = 400$ K[a]		
223.77	100.3337	28	244.90	103.3281	59	306.91	105.7644	57
203.78	100.6460	27	222.61	103.6199	44	278.44	106.0920	50
185.17	100.9319	31	201.55	103.8952	47	264.21	106.2538	53
168.17	101.1906	33	182.49	104.1430	50	238.65	106.5414	49
152.72	101.4244	37	165.17	104.3668	53	215.53	106.8010	57
132.32	101.7307	38	149.59	104.5666	56	194.67	107.0336	58
120.13	101.9129	44	128.85	104.8314	56	175.75	107.2439	60
104.02	102.1523	45	122.47	104.9128	56	151.07	107.5162	61
94.41	102.2943	46	110.79	105.0609	62	143.51	107.5998	64
77.91	102.5370	50	95.40	105.2557	61	129.69	107.7506	65
64.26	102.7366	52	82.22	105.4221	67	111.61	107.9489	66
50.52	102.9373	56	74.43	105.5205	65	100.96	108.0655	71
			70.77	105.5665	66	86.98	108.2174	72
			58.03	105.7265	68	75.11	108.3472	78
			50.00	105.8267	71	61.86	108.4911	81
						51.14	108.6076	76
$T = 360$ K[a]			$T = 380$ K[a]			$T = 420$ K[a]		
220.45	100.3863	38	243.42	103.3468	52	309.89	108.8377	95
200.66	100.6953	30	220.80	103.6445	48	293.98	108.9957	79
182.21	100.9772	33	209.67	103.7891	44	264.05	109.2874	76
165.49	101.2325	39	189.63	104.0504	53	249.82	109.4251	83
150.26	101.4629	39	171.57	104.2837	47	224.48	109.6708	83
130.22	101.7635	44	147.67	104.5915	54	191.33	109.9905	86
118.27	101.9415	46	127.00	104.8557	58	171.90	110.1761	86
107.51	102.1017	51	120.67	104.9361	55	146.43	110.4197	88
93.14	102.3140	50	109.09	105.0838	60	131.52	110.5618	102
76.99	102.5520	53	98.62	105.2154	66	118.11	110.6889	91
63.71	102.7463	56	84.88	105.3894	69	106.17	110.8021	91
50.29	102.9420	54	73.05	105.5378	71	95.29	110.9053	95
			62.86	105.6663	74	85.59	110.9973	98
			48.98	105.8398	72	72.93	111.1167	93
						62.13	111.2189	105
						50.19	111.3322	100

[a] Indicates isotherm contains corrected sound speeds.

4. RESULTS

At each temperature and pressure, two longitudinal and two radial modes were used to compute values of the speed of sound. The weighted mean of these four values and their relative standard deviation $\sigma[u]/u \times 10^6$ with coverage factor of $k = 1$ are listed in Table I. The listed values at 360 K and higher temperatures have been corrected as described in Section 5. A total of 146 state points are reported along 10 isotherms. Redundant data were taken on the isotherms at 360 and 380 K to demonstrate reproducibility of our experimental method and the corrections for the reaction of the WF_6.

5. CORRECTIONS

Figure 3 (top) shows the time lines or histories of the speed-of-sound measurements taken at 380 K that were used to deduce the corrections for the two pressure-dependent 380 K isotherms. Similar time lines were followed for the other corrected isotherms. Three separate samples of WF_6 were studied. The first sample was loaded to 50 kPa, and the speed of sound was monitored with time while holding the temperature constant. This is shown as interval A in Fig. 3 (top). The speed of sound was extrapolated back to the time immediately after loading (t_0), and this value was assumed to be the correct value of u for pure WF_6 at 380 K and 50 kPa. The resonator was then evacuated and reloaded with a fresh sample at 240 kPa. The temperature and pressure were held constant, and the speed of sound was monitored during interval B. The pressure was then dropped in successive steps of 50 kPa, and the speed of sound was measured during interval C as a function of pressure and time. The pressure was then again held constant at 50 kPa and the speed of sound measured as a function of time every 20 min for approximately 300 min during interval D. The resonator was again evacuated and reloaded to 240 kPa with the third sample of sample gas. The speed of sound was measured again as the pressure was dropped in successive steps to 50 kPa during interval E. The data obtained during intervals C and E were corrected and used to determine the thermophysical properties. The data obtained during intervals A, B, and D were used to correct the data otained during the intervals C and E.

Figure 3 (bottom) shows the change in the speed of sound during the three intervals A, B, and D, when the pressure was held constant. In each case, the change in sound speed was a linear function of time. The slopes of the three lines are $\dot{u}/u = 6.7 \times 10^{-9}\ \mathrm{s}^{-1}$ for A, $\dot{u}/u = 1.05 \times 10^{-9}\ \mathrm{s}^{-1}$ for B, and $\dot{u}/u = 7.2 \times 10^{-9}\ \mathrm{s}^{-1}$ for D, where $\dot{u} = [u(t) - u(t_0)]/(t - t_0)$. Within

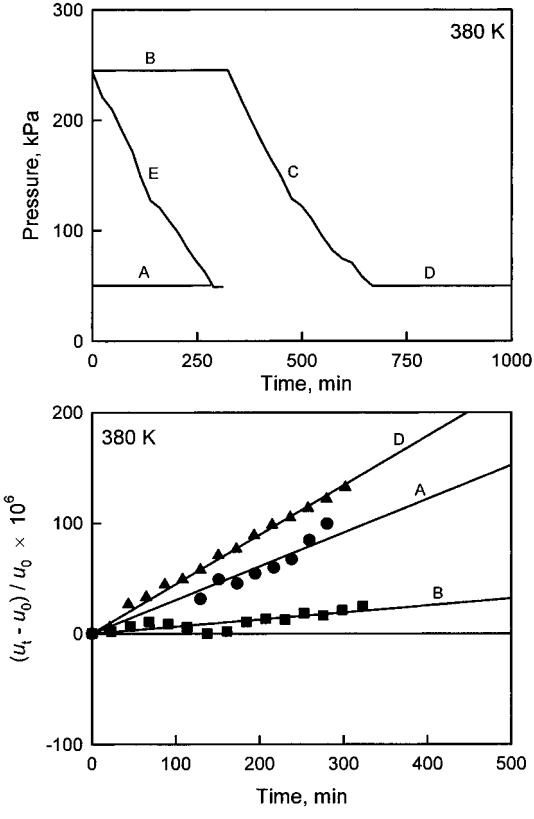

Fig. 3. Top: Time lines or histories of the 380 K measurements. Bottom: Time dependence of the speed of sound during intervals A, B, and D, while the pressure was held constant.

the uncertainties, the slope of B is equal to the slope of D scaled by the ratio of the pressures (240 kPa/50 kPa). This is consistent with a reaction rate which is independent of the density, as if the WF_6 were reacting at an interior surface of the resonator. If the rate limiting factor were the surface area of the container, the mole fraction of the products would accumulate at a rate proportional to P^{-1}, which was, in fact, observed. The slopes for A and D are not identical. This implies that the reaction rate was a function of each sample studied, as well as a function of temperature and pressure. Thus, each loading of the resonator required an independent determination of the correction parameters. Each isotherm was corrected by assuming a constant and density independent reaction rate using the

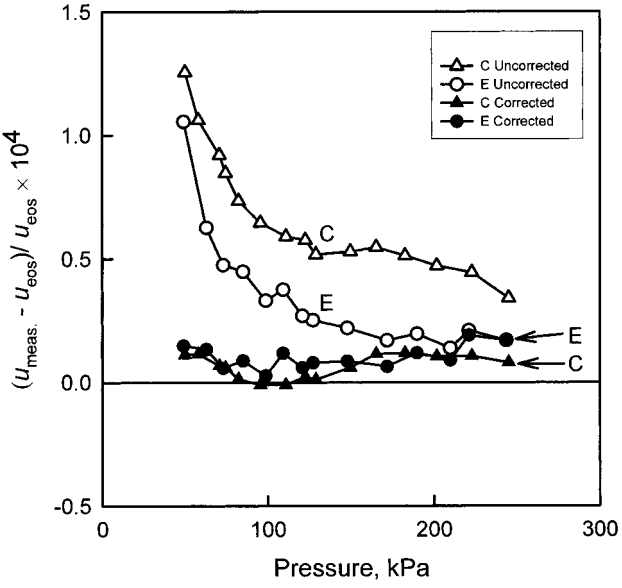

Fig. 4. The fractional deviations of the corrected and uncorrected speed-of-sound data from the equation of state presented in Section 8. The labels C and E refer to the intervals in Fig. 3.

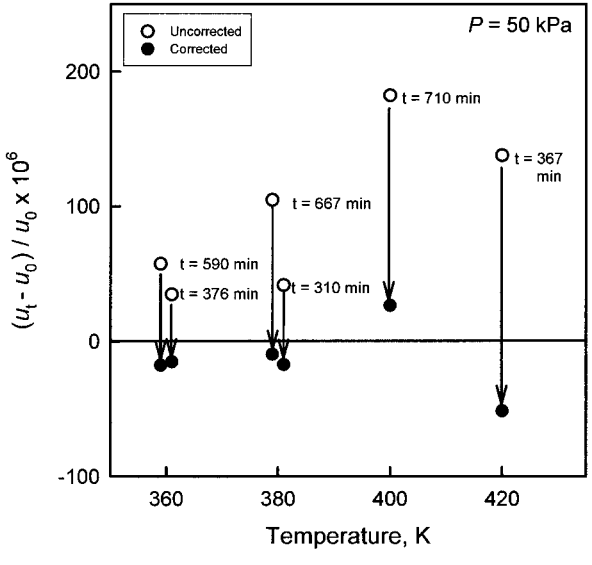

Fig. 5. The corrected and the uncorrected speed-of-sound data at 50 kPa.

unique slope determined for that sample of gas while it was held at 50 kPa. The corrections were applied to the isotherms at 360, 380, 400, and 420 K, and the corrected speeds of sound are reported in Table I.

Figure 4 shows the two 380 K isotherms before and after applying the correction. The base line is our equation of state that is presented in Section 8. After correction, the data acquired during intervals E and C agree within their combined experimental uncertainties.

Figure 5 shows the magnitude of the corrections at 50 kPa for various intervals at four temperatures. The corrections were largest at 50 kPa; they were much smaller at the higher pressures because there was more gas present and because the time spent at each pressure was much shorter. In all cases, the corrected data are correlated by our virial equation of state within experimental uncertainties.

6. IDEAL-GAS HEAT CAPACITIES

The ideal-gas heat capacity is determined by fitting each isotherm with the acoustic virial equation of state,

$$u^2 = \frac{\gamma^0 RT}{m}\left(1 + \frac{\beta_a p}{RT} + \frac{\gamma_a p^2}{RT} + \frac{\delta_a p^3}{RT} + \cdots\right) \tag{1}$$

where m is molar mass, R is the universal gas constant, T is temperature in kelvin, $\gamma^0(T) = C_p^0(T)/C_v^0(T)$ is the zero-pressure limit of the heat-capacity ratio, and β_a, γ_a, and δ_a are the temperature-dependent acoustic virial coefficients. The ideal-gas heat capacity is obtained from the zero-pressure intercept of Eq. (1) through the relation $C_p^0(T)/R = \gamma^0/(\gamma^0 - 1)$. This analysis results in a value for C_p^0 for each isotherm which are listed in Table II. The values presented in Table II have a relative standard uncertainty of better than 0.1%. Figure 6 (top) shows the C_p^0 values given in Table II as filled circles along with literature values of C_p^0 calculated from

Table II. Ideal-Gas Heat Capacities Determined for Each Isotherm

T (K)	290	300	310	320	330	340	360[a]	380[a]	400[a]	420[a]
C_p^0/R	14.22	14.43	14.62	14.78	14.96	15.10	15.43 15.42	15.67 15.68	15.92	16.13

[a] Obtained from a fit to the isotherms corrected as described in Section 5.

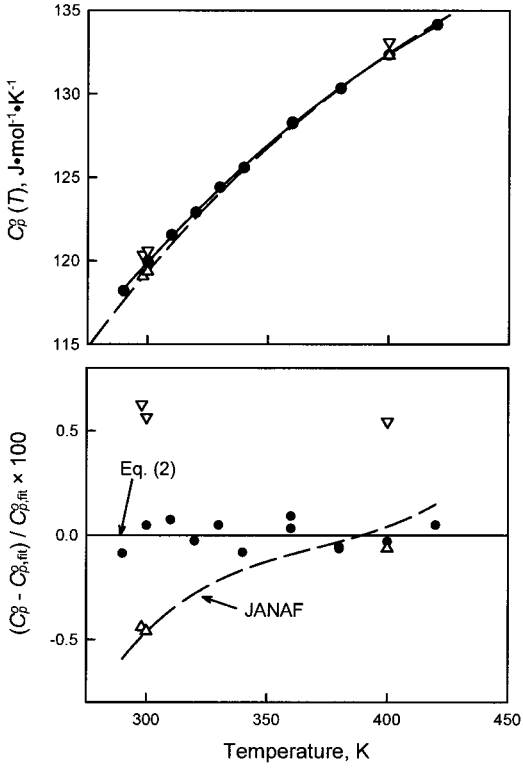

Fig. 6. Top: The ideal-gas heat capacity C_p^0 as a function of temperature. Bottom: Percentage deviations from $C_{p,\,fit}^0$ given by Eq. (2). (●) Present values; (---) Ref. 12; (△) Ref. 14; (▽) Ref. 15.

spectroscopic data. The $C_p^0(T)/R$ results for each isotherm were fit by the polynomial function of the temperature,

$$C_P^0/R = 5.207 + 0.04251(T/\mathrm{K}) - 3.931 \times 10^{-1}(T/\mathrm{K})^2, \quad 290\ \mathrm{K} \leqslant T \leqslant 420\ \mathrm{K} \tag{2}$$

Equation (2) is valid only over our experimental temperature range 290 K $\leqslant T \leqslant$ 420 K. Figure 6 (bottom) shows the deviations of the $C_p^0(T)/R$ values reported in Table II from those calculated from Eq. (2). Nearly all the heat capacity data are within 0.1% of the fitted function. The dashed line comes from the JANAF (Joint Army Navy Air Force) tables [12] which calculate $C_p^0(T)$ from spectroscopic data. JANAF claims no better

than 1.0% relative standard uncertainty for WF_6 [13]. Two other published estimated $C_p^0(T)$ values [14, 15] are also included.

7. HARD-CORE SQUARE-WELL MODEL (HCSW)

The virial equation of state is given by

$$P = RT\rho[1 + B(T)\,\rho + C(T)\,\rho^2 + D(T)\,\rho^3 + \cdots] \tag{3}$$

Gillis and Moldover [4] have discussed in detail how the hard-core square-well (HCSW) intermolecular potential model can be used to deduce the virial equation of state from speed-of-sound data. They provide exact thermodynamic equations which relate the density virial coefficients, their temperature derivatives, and γ^0 to the acoustic virial coefficients in Eq. (1). We used their results with parameterized representations of $B(T)$ and $C(T)$. For the HCSW model potential the representations of $B(T)$ and $C(T)$ are algebraic,

$$B(T) = b_0[1 - (\lambda^3 - 1)\,\Delta] \tag{4}$$

$$\begin{aligned} C(T) &= \tfrac{1}{8}b_o^2(5 - c_1\Delta - c_2\Delta^2 - c_3\Delta^3) \\ c_1 &= \lambda^6 - 18\lambda^4 + 32\lambda^3 - 15 \\ c_2 &= 2\lambda^6 - 36\lambda^4 + 32\lambda^3 + 18\lambda^2 - 16 \\ c_3 &= 6\lambda^6 - 18\lambda^4 + 18\lambda^2 - 6 \end{aligned} \tag{5}$$

where $\Delta = e^{\varepsilon/(k_B T)} - 1$, k_B is Boltzmann's constant, b_o is the molar volume of the hard core ($b_o = \frac{2}{3}\pi N_A \sigma^3$), and N_A is Avogadro's constant. The adjustable parameters in these expressions are ε, the well depth; σ, the hard core diameter; and λ, the ratio of the width of the well to σ. The present data extend to high enough pressure (density) to require both the second and the third virial coefficients. We follow Ref. 4 in using two sets of values of b_o, ε, and λ; one for $B(T)$ and one for $C(T)$.

To fit the data, the ideal-gas heat capacity was fixed at the values given by Eq. (2) and the six parameters, b_o, ε, and λ for $B(T)$ and b_o, ε,

Table III. Parameters for HCSW Equations of State Deduced from $u(T, P)$ Measurements

	b_0 ($m^3 \cdot mol^{-1}$)	λ	ε/k_B (K)
$B(T)$ ($cm^3 \cdot mol^{-1}$)	1.20335×10^{-4}	1.39281	492.89
$C(T)$ ($cm^3 \cdot mol^{-1}$)^2	2.40315×10^{-4}	1.25777	495.65

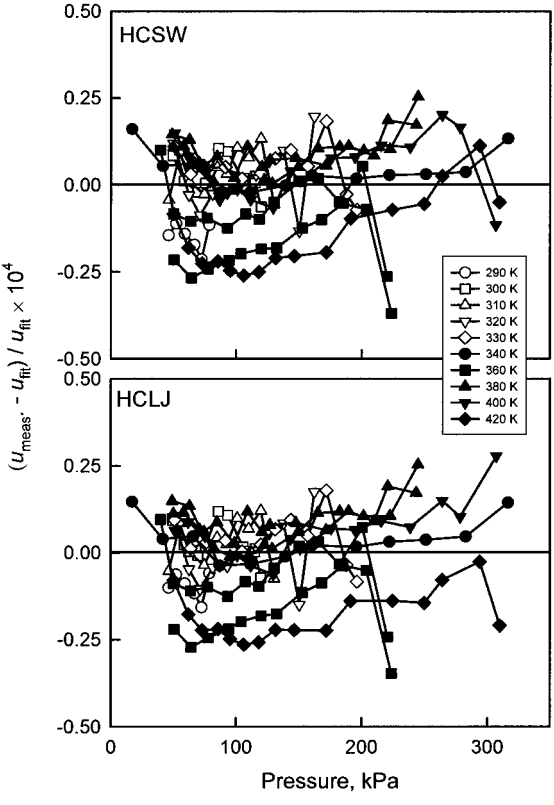

Fig. 7. Fractional deviations of the speed-of-sound data from fitted values. Top: HCSW equation of state. Bottom: HCLJ equation of state.

and λ for $C(T)$, were allowed to vary. The resulting parameters are listed in Table III. Figure 7 (top) shows the deviations of the measured sound speeds in WF_6 from those calculated from the determined HCSW virial equation of state. All of our reported sound speeds are fitted to within $\pm 0.005\%$. The fit had 140 df, v, and χ^2/v was 0.07, where $\chi^2 = \sum_i [f(x_i) - f_i]^2/\sigma_f^2$, and $f(x_i) = = u^2(P, T)$.

8. HARD-CORE LENNARD–JONES MODEL (HCLJ)

The HCLJ analysis is similar to the HCSW analysis; however, it was more difficult to implement. We had to perform numerical integrations at each temperature to determine the virial coefficients and their temperature derivatives. Trusler [16] performed a similar analysis on propane using the

Maitland–Smith potential [17]. We used the hard-core Lennard–Jones 6–12 potential [18] given by

$$\varphi(r_{ij}) = 4\varepsilon \left\{ \left(\frac{\sigma - 2a}{r_{ij} - 2a} \right)^{12} - \left(\frac{\sigma - 2a}{r_{ij} - 2a} \right)^{6} \right\} \tag{7}$$

where r_{ij} is the intermolecular separation between molecule i and molecule j, ε is the well depth, σ is the value of r_{ij} where $\varphi(r)$ crosses zero, and a is the radius of the hard core. This potential has three adjustable parameters: ε, σ, and a. In the case of WF_6 this potential resulted in a superior fit than the Maitland–Smith potential. We calculated the classical second and third virial coefficients and their temperature derivatives [19, 20] using an automatic adaptive quadrature routine [21], where one can specify the desired accuracy, which we set to 10^{-4}. The calculation of the third virial coefficient requires inclusion of three-body contributions. This adds a fourth adjustable parameter, ν_{123}. Following Trusler [16], we used the Axilrod–Teller triple–dipole term [22],

$$\varphi(r_{123}) = \frac{\nu_{123}(1 + \cos\theta_1 \cos\theta_2 \cos\theta_3)}{(r_{12}^3 r_{13}^3 r_{23}^3)^{-1}} \tag{8}$$

where ν_{123} is the dispersion coefficient and θ_i is defined as the angle subtended at molecule i by molecules j and k. This is the first term in the three-body corrections to the dispersion energy for monatomic species. The integral equations providing the second and third virial coefficients for spherically symmetric molecules are given by

$$B(T) = -2\pi N_A \int_0^\infty f_{12} r_{12}^2 \, dr_{12} \tag{9}$$

$$C(T) = -\frac{8\pi^2 N_A^2}{3} \int_0^\infty \int_0^\infty \int_{|r_{12} - r_{13}|}^{|r_{12} + r_{13}|} (f_{12} f_{13} f_{23} - e_{12} e_{13} e_{23} f_{123}) \times r_{12} r_{13} r_{23} \, dr_{12} \, dr_{13} \, dr_{23} \tag{10}$$

where N_A is Avagadro's number, r_{ij} is the distance between molecule i and molecule j, $e_{ij} = \exp\{-\varphi(r_{ij})/kT\}$, $f_{ij} = e_{ij} - 1$, and $f_{ijk} = \exp\{-\varphi(r_{ijk})/kT\} - 1$. Equations (9) and (10) allow us to calculate the second and third density virial coefficients, and their temperature derivatives, for a given intermolecular potential at a given temperature. With $C_p^0(T)/R$ given by Eq. (2), only four potential parameters, ε, σ, a, and ν_{123} are required to fit the $u(T, P)$ data. Initial estimates of ε, σ, and a were determined by fitting the HCLJ second virial coefficient to that of the HCSW model. These parameters were fixed, and an initial value for ν_{123} was determined by

Table IV. Parameters for the HCLJ Potential Model Deduced from $u(T, P)$ Measurements

a	0.10216 nm
σ	0.49077 nm
ε/k_B	690.06 K
ν_{123}	0.11145 K · nm^9

fitting only ν_{123} to the third virial values determined from the HCSW method. Then all four parameters were allowed to vary while fitting to the $u(T, P)$ measurements. The resulting parameters are given in Table IV. Figure 7 (bottom) shows the deviations of the measured sound speeds from those calculated from the deduced HCLJ equation of state. As in the case of the HCSW model, all sound-speed measurements are fitted within $\pm 0.005\,\%$. The fit had 142 df, ν, and χ^2/ν was 0.06.

Figure 8 (top) shows the second virial coefficient deduced for the two models. The barely visible dashed line is the HCSW model, and the solid line is the HCLJ model. Also shown are the previously published measurements of $B(T)$. Both representations of $B(T)$ pass through previous measurements, mostly within the latter's claimed uncertainties. Figure 8 shows that our representation of $B(T)$ extrapolates extemely well outside our experimental temperature range. Figure 8 (bottom) shows the third virial coefficient deduced from this work. The differences between the HCSW and the HCLJ are observable. The HCLJ model behaves more realistically at the higher temperatures, tending toward zero, while the HCSW model levels off at a constant. There are no previously published values of $C(T)$ that may be compared with our results.

9. INTERPOLATION ROUTINE

The computation of the second and third virial coefficients and their temperature derivatives from Eqs. (9) and (10) using the four potential parameters is a numerically intensive process and is not convenient for repetitive calculations. Again, following the lead of Trusler [16], we provide a look-up table for the second and third virial coefficients and their first two temperature derivatives, along with a preferred method of interpolation. In the look-up table, a substitution of variables has been performed. The temperature is replaced by a reduced reciprocal temperature $\tau = \varepsilon/kT$, where $T(dB/dT) = -\tau(dB/d\tau)$ and $T^2(d^2B/dT^2) = \tau^2(d^2B/d\tau^2) + 2\tau(dB/d\tau)$. Table IV provides the virial coefficients in reduced (unitless) form, where $B^*(T) = B(T)/b_0$ and $C^*(T) = C(T)/b_0^2$, where $b_0 = \frac{2}{3}\pi N_A \sigma^3$. Table V spans the reduced temperature range $0.3 \leqslant \tau \leqslant 3.0$ which corresponds

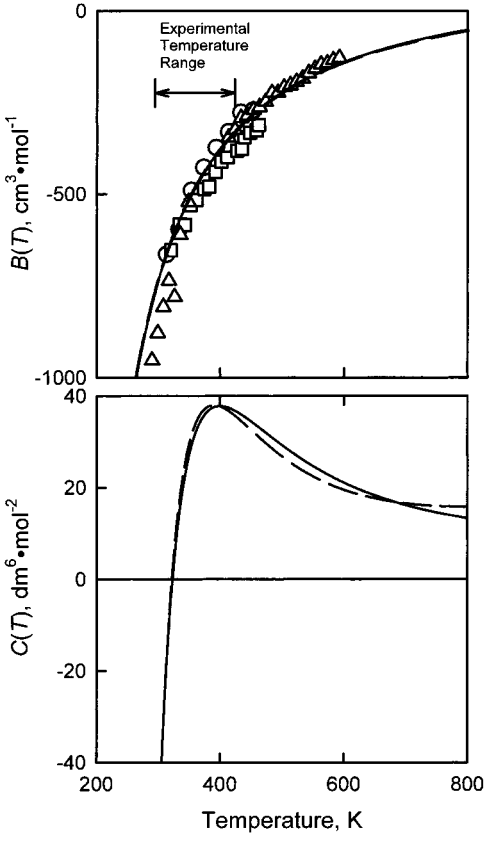

Fig. 8. Top: The second density virial coefficient. Bottom: The third density virial coefficient. (—) HCLJ model; (– – –) HCSW model; (○) Ref. 27; (□) Ref. 28; (△) Ref. 3.

to 196 to 1966 K. This range greatly exceeds our experimental temperature range; however, the extrapolated virial coefficients are reliable, as demonstrated by our experience with CF_4 and C_2F_6 [5] and Trusler's experience with C_3H_8 [16]. The recommended interpolation of $B^*(t)$ and $C^*(t)$ or their derivatives at τ between adjacent points at τ_1 and τ_2 is the cubic polynomial $f(t)$, such that

$$
\begin{aligned}
f(\tau) &= a(\tau-\tau_1) + b(\tau-\tau_2) + \{c(\tau-\tau_1) + d(\tau-\tau_2)\}(\tau-\tau_1)(\tau-\tau_2) \\
a &= f(\tau_2)/\Delta\tau, \qquad c = \{f'(\tau_2)/(\Delta\tau)^2\} - \{(a+b)/(\Delta\tau)^2\} \\
b &= -f(\tau_1)/\Delta\tau, \qquad d = \{f'(\tau_1)/(\Delta\tau)^2\} - \{(a+b)/(\Delta\tau)^2\}
\end{aligned}
\tag{13}
$$

Table V. Reduced Virial Coefficients of WF_6 and Their Derivatives with Reduced Temperature Deduced from the HCLJ Model

τ	$B(\tau)^*$	$\partial B(\tau)^*/\partial\tau$	$\partial^2 B(\tau)^*/\partial\tau^2$	$\partial^3 B(\tau)^*/\partial\tau^3$	$C(\tau)^*$	$\partial C(\tau)^*/\partial\tau$	$\partial^2 C(\tau)^*/\partial\tau^2$	$\partial^3 C(\tau)^*/\partial\tau^3$
0.3	0.052130	−0.120004	−0.151650	0.493305	0.003965	−0.000457	0.005761	0.086539
0.4	0.039435	−0.133420	−0.122055	0.161481	0.003961	0.000468	0.012096	0.047201
0.5	0.025503	−0.145061	−0.112720	0.042341	0.004075	0.001882	0.015948	0.031733
0.6	0.010437	−0.156228	−0.111538	−0.012659	0.004348	0.003620	0.018654	0.022917
0.7	−0.005747	−0.167503	−0.114472	−0.043535	0.004807	0.005588	0.020575	0.015489
0.8	−0.023078	−0.179205	−0.119907	−0.064042	0.005470	0.007709	0.021719	0.007087
0.9	−0.041609	−0.191544	−0.127124	−0.079770	0.006351	0.009900	0.021907	−0.003877
1.0	−0.061413	−0.204678	−0.135789	−0.093297	0.007449	0.012048	0.020809	−0.018890
1.1	−0.082576	−0.218745	−0.145754	−0.105942	0.008754	0.014003	0.017938	−0.039639
1.2	−0.105197	−0.233871	−0.156973	−0.118447	0.010236	0.015554	0.012621	−0.068202
1.3	−0.129389	−0.250181	−0.169455	−0.131276	0.011842	0.016415	0.003950	−0.107234
1.4	−0.155277	−0.267805	−0.183249	−0.144743	0.013483	0.016192	−0.009287	−0.160158
1.5	−0.182999	−0.286878	−0.198433	−0.159089	0.015027	0.014353	−0.028692	−0.231415
1.6	−0.212706	−0.307541	−0.215103	−0.174513	0.016276	0.010179	−0.056372	−0.326775
1.7	−0.244565	−0.329952	−0.233377	−0.191197	0.016953	0.002711	−0.095097	−0.453729
1.8	−0.278760	−0.354275	−0.253390	−0.209313	0.016667	−0.009328	−0.148492	−0.622009
1.9	−0.315490	−0.380693	−0.275294	−0.229038	0.014879	−0.027633	−0.221294	−0.844249
2.0	−0.354975	−0.409402	−0.299257	−0.250552	0.010858	−0.054438	−0.319682	−1.136843
2.1	−0.397454	−0.440619	−0.325470	−0.274047	0.003611	−0.092688	−0.451709	−1.521058
2.2	−0.443190	−0.474578	−0.354140	−0.299730	−0.008189	−0.146247	−0.627858	−2.024473
2.3	−0.492470	−0.511537	−0.385496	−0.327823	−0.026316	−0.220180	−0.861758	−2.682849
2.4	−0.545607	−0.551775	−0.419793	−0.358568	−0.053123	−0.321108	−1.171123	−3.542546
2.5	−0.602944	−0.595602	−0.457307	−0.392227	−0.091722	−0.457679	−1.578961	−4.663664
2.6	−0.664858	−0.643354	−0.498345	−0.429089	−0.146219	−0.641169	−2.115141	−6.124106
2.7	−0.731758	−0.695400	−0.543242	−0.469470	−0.222005	−0.886265	−2.818427	−8.024865
2.8	−0.804094	−0.752144	−0.592368	−0.513715	−0.326156	−1.212084	−3.739113	−10.496874
2.9	−0.882358	−0.814028	−0.646127	−0.562203	−0.467933	−1.643488	−4.942447	−13.709900
3.0	−0.967087	−0.881538	−0.704963	−0.615349	−0.659439	−2.212788	−6.513060	−17.884099

where $f' = df/d\tau$ and $\Delta\tau = \tau_2 - \tau_1$. To allow the calculation of the second temperature derivative, the third temperature derivative is included in Table V.

10. TRANSPORT PROPERTIES

The HCLJ intermolecular potential deduced for WF_6 in Section 8 is a reasonable model for computing the dilute-gas properties of WF_6. The HCLJ intermolecular potential represents a spherically symmetric average over all collision orientations, which for an octahedral geometry is a very good approximation. However, experience has shown that thermodynamic data alone are not sufficient to determine the details of an intermolecular potential. Nevertheless, the potential allows reasonable estimates of viscosities and thermal conductivities from the kinetic theory of gases [23].

We calculated the viscosity of WF_6 from the HCLJ intermolecular potential. The following empirical function was fitted to the results:

$$\eta(\mu\text{Pa}\cdot\text{s}) = 4.067 + 0.0492(T/\text{K}) - 5.102\times10^{-6}(T/\text{K})^2, \qquad 220\text{ K} \leqslant T \leqslant 1000\text{ K} \tag{14}$$

Equation (14) represents the calculated viscosities to within 0.2% of η over the temperature range 220 K $\leqslant T \leqslant$ 1000 K. Figure 9 (top) shows that the viscosity calculated from our HCLJ potential agrees with the one available set of experimental viscosities [6]. We have claimed that viscosities estimated in this manner are expected to be within 10% of their true values. Figure 9 (bottom) shows that we reproduced the only available experimental viscosity data set to better than 5%, supporting this assertion. Viscosities calculated from the HCLJ potential determined for CF_4 and C_2F_6 [5] from $u(T, P)$ data were approximately 5% below the measured values in both cases. Similarly, the viscosity of propane predicted by the Maitland–Smith potential that Trusler obtained from his $u(T, P)$ data deviates from measured viscosities by +4.2% at 200 K, −1.6% at 300 K, and −6.5% at 500 K [16].

The thermal conductivity l of dilute gases can be estimated from the viscosity and the constant-volume ideal-gas heat capacity with the Eucken [24] approximation,

$$[\lambda]_{\text{Eucken}} = \frac{15}{4}\frac{R}{M}\eta\left(\frac{4}{15}\frac{C_v}{R} + \frac{3}{5}\right) \tag{15}$$

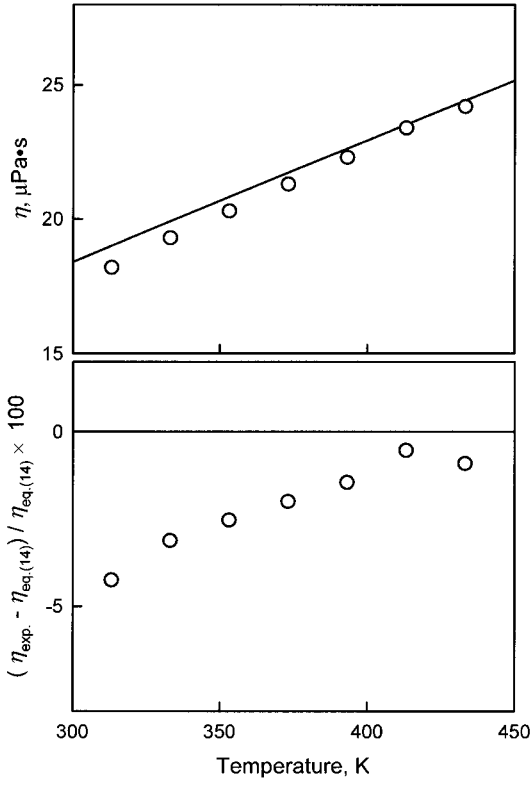

Fig. 9. Top: The viscosity of WF_6 calculated from the HCLJ potential and fit to Eq. (14) is shown as the solid line. The measurements of Ref. 6 are shown as open circles. Bottom: The fractional deviations of measurements of Ref. 6 from Eq. (14).

We have calculated λ from Eq. (15) using Eqs. (2) and (14) and values of C_p^0 from the JANAF [12] tables. The following simple polynomial was fitted to the resulting values of λ:

$$\lambda^\circ\,(\mathrm{W\cdot m^{-1}\cdot K^{-1}}) = -1.606\times10^{-3} + 3.382\times10^{-5}(T/\mathrm{K}) - 5.833\times10^{-9}(T/\mathrm{K})^2, \qquad 220\ \mathrm{K} \leqslant T \leqslant 1000\ \mathrm{K} \quad (16)$$

The values of λ from Eq. (16) have relative standard uncertainties of the order of 10%. They come from the relative standard uncertainty of the viscosity ($\sim$5%), the Eucken approximation ($\sim$10%) [25], and C_v

($\sim$1%). In future work, we will use an acoustic technique to measure the thermal conductivity and the viscosity [26]. This will allow us to test our transport property estimates. Also in future work, we will examine mixtures of process gases with carrier gases such as argon, helium, and nitrogen. In these cases it will be necessary to fit the interaction potentials from which we will estimate the diffusion coefficient. Diffusion coefficients are required to model processes where the rate-limiting step is the diffusion of a reactant from a carrier gas to a hot silicon surface.

ACKNOWLEDGMENT

This work has been supported in part by the National Semiconductor Metrology Program.

REFERENCES

1. *Zahlenwerte und Funktionen*, *Band II*, *Teil 2*, Landolt–Börnstein (Springer-Verlag, Berlin/Göttingen/Heidelberg, 1960).
2. E. F. Westrum, *Pure Appl. Chem.* **8**:187 (1964).
3. V. V. Malyshev, *Teplofiz. Vysokikh Temp.* **11**:1010 (1973).
4. K. A. Gillis and M. R. Moldover, *Int. J. Thermophys.* **17**:1305 (1996).
5. J. J. Hurly, *Int. J. Thermophys.* **20**:455 (1999).
6. A. Heintz and R. N. Lichtenthaler, *Ber. Bunsenges Phys. Chem.* **80**:962 (1976).
7. A. R. H. Goodwin and M. R. Moldover, *J. Chem. Phys.* **95**:5236 (1991).
8. K. A. Gillis, *Int. J. Thermophys.* **18**:73 (1997).
9. K. A. Gillis, *Int. J. Thermophys.* **15**:821 (1994).
10. K. A. Gillis, A. R. H. Goodwin, and M. R. Moldover, *Rev. Sci. Instrum.* **62**:2213 (1991).
11. J. W. S. Rayleigh, *Theory of Sound* (Dover, New York, 1945).
12. M. W. Chase, C. A. Davies, J. R. Downey, D. J. Frurip, R. A. McDonald, and A. N. Syverud, *J. Phys. Chem. Ref. Data* **14**:1166 (1985).
13. M. W. Chase, Private Communication (National Institute of Standards and Technology, Gaithersburg, MD, 1999).
14. G. Nagarajan, *Bull. Soc. Chim. Belg.* **71**:77 (1962).
15. G. Nagarajan and D. C. Brinkley, *Z. Naturforsch.* **26A**:1658 (1977).
16. J. P. M. Trusler, *Int. J. Thermophys.* **18**:635 (1997).
17. C. G. Maitland and E. B. Smith, *Chem. Phys. Lett.* **22**:443 (1973).
18. T. Kihara, *Rev. LMod. Phys.* **25**:831 (1953).
19. E. A. Mason and T. H. Spurling, *The Virial Equation of State* (Pergamaon Press, Oxford, 1969).
20. R. J. Dulla, J. S. Rowlinson, and W. R. Smith, *Mol. Phys.* **21**:229 (1971).
21. R. F. Boisvert, S. E. Howe, D. K. Kahaner, and J. L. Springmann, *The Guide to Available Mathematical Software*, NISTIR 90-4237 (1990).
22. B. M. Axilrod and E. J. Teller, *J. Chem. Phys.* **11**:299 (1943).
23. J. O. Hirschfelder, C. F. Curtiss, and R. B. Bird, *Molecular Theory of Gases and Liquids* (Wiley, New York, 1954).

24. A. Eucken, *Phys. Z* **14**:324 (1913).
25. R. C. Reid, J. M. Prausnitz, and T. K. Sherwood, *The Properties of Gases and Liquids*, 3rd. ed. (McGraw–Hill, New York, 1977).
26. K. A. Gillis, J. B. Mehl, and M. R. Moldover, *Rev. Sci. Instrum.* **67**:1850 (1996).
27. P. Morizot, J. Ostorero, and P. Plurien, *J. Chem. Phys.* **70**:1582 (1973).
28. A. Heintz and R. N. Lichtenthaler, *Ber. Bunsenges Phys. Chem.* **80**:962 (1976).